https://doi.org/10.5194/egusphere-2026-6875
Preprint. Discussion started: 19 November 2026
© Author(s) 2026. CC BY 4.0 License.

EarthMesh: A Multi-Scale Unstructured Mesh Generation Tool for Earth System Models

Rui Zhang[1], Zhongwang Wei[1*], Yinhai Luo[2], Hanwen Fan[3], Qingchen Xu[1], Shupeng Zhang[1], Nan Wei[1], Xingjie Lu[1], Lu Li[1], Huan Yuan[1], Xianxiang Li[1], Shaofeng Liu[1], Wei Shangguan[1], Yongjiu Dai[1*]

[1]School of Atmospheric Sciences, Sun Yat-sen University, Zhuhai, China

[2]Laboratory of Middle Atmosphere and Global Environment Observation, Institute of Atmospheric Physics, Chinese Academy of Sciences, Beijing, China

[3]Commercial Aircraft Corporation of China Ltd Meteorological Research Center, Commercial Aircraft Corporation of China Ltd Shanghai Aircraft Flight Test Co., Ltd., Shanghai, China

Correspondence to: Zhongwang Wei (weizhw6@mail.sysu.edu.cn); Yongjiu Dai (daiyj6@mail.sysu.edu.cn)

Key points

- EarthMesh refines unstructured meshes using physical criteria, user-defined regions, or both.
- Transition construction and spring adjustment improve local simulation accuracy.
- Post-processing drivers create input files for atmospheric, oceanic, and land models.

Abstract

Variable-resolution meshes (VRMs) on unstructured grids direct resolution to regions where local processes need finer representation, but producing solver-ready meshes across Earth system model (ESM) components remains difficult. Existing tools typically focus on a single component, leaving users to write post-processing scripts for each solver. Here we present EarthMesh, a workflow for generating triangular and dual-

https://doi.org/10.5194/egusphere-2026-6875
Preprint. Discussion started: 19 November 2026
© Author(s) 2026. CC BY 4.0 License.

polygonal meshes on the sphere and preparing them for atmospheric, oceanic, and land-surface models. EarthMesh starts with an icosahedral triangular mesh, refines cells using user-defined regions, physical criteria such as land cover types and leaf area index (LAI), or both, and reconstructs conforming transition rows while keeping vertex valence between 5 and 7. A modified spring-dynamics optimization reduces the number of obtuse triangles within transition areas. Model-specific drivers then produce the input files required by MPAS-A, FVCOM, and CoLM2024. In idealized MPAS-A baroclinic-wave and FVCOM geostrophic-eddy tests, the VRMs reproduce the fine-scale structures of uniform high-resolution runs within the refined regions, without spurious signals at the transition zones, while using about 8% and 44-47% of the high-resolution cell count, respectively. In a CoLM2024 runoff experiment over the eastern United States, refinement driven by LAI variability and land-cover diversity improves monthly runoff skill over 55% of the domain (62% for uniform refinement) with 28% of the high-resolution cells. These results provide practical guidance on transition width, refinement criteria, and dual-mesh construction for different ESM components.

1 Introduction

Earth system models (ESMs) need fine horizontal resolution to represent localized processes such as atmospheric baroclinic waves, ocean eddies, and surface hydrological heterogeneity (Chassignet and Xu, 2021; Tesfa et al., 2020; Zängl et al., 2022), while their prohibitive computational cost severely limits domain size, ensemble size, and integration length. This trade-off has motivated a growing number of studies which use models formulated on nested (Debreu and Blayo, 2008) or generalized curvilinear meshes (Wei et al., 2016) to achieve local high-resolution in regions of interest. Variable-resolution meshes (VRMs) on unstructured grids, including Delaunay triangulations and dual Voronoi polygons, offer an alternative. Compared with traditional nested or generalized curvilinear meshes, unstructured grids offer more flexibility for implementing locally refined resolution (Hagos et al., 2013). Their refined areas can be of arbitrary shape, and their resolution can be varied according to the desired function (Sein et al., 2016; 2017). These advantages have led to the rapid

https://doi.org/10.5194/egusphere-2026-6875
Preprint. Discussion started: 19 November 2026
© Author(s) 2026. CC BY 4.0 License.

development of unstructured grid models (Walko and Avissar, 2008; Ringler et al., 2013; Wang et al., 2014; Zängl et al., 2015) and their use in atmospheric, oceanic, and land-surface modeling (Marsh et al., 2020; Song et al., 2023; Xu et al., 2021).

However, the distribution of grid resolution is directly related to simulation accuracy, making the mesh design process challenging (Hoch et al., 2020; Sein et al., 2016). Automated tools that make unstructured mesh generation easier and more reproducible are therefore valuable for the Earth system modeling community (Engwirda, 2017; Fan et al., 2024; Roberts et al., 2019). However, existing automated tools usually generate unstructured grids around the requirements of a single model class. This is because atmospheric, oceanic, and land surface models have distinct priorities in unstructured mesh generation. For instance, atmospheric simulation demands high geometric and topological quality (Zhou et al., 2020). The direct refinement method of Walko and Avissar (2011), which builds conforming transition rows on icosahedral triangular grids, provides a fast generation approach for high-quality unstructured grids. The MPI-SCVT algorithm (Jacobsen et al., 2013) distributes a set of vertices over the spherical surface and iteratively smooths until a high-quality Voronoi tessellation is obtained. The JIGSAW-GEO tool produces locally orthogonal staggered grids for global atmospheric/oceanic circulation modeling (Engwirda, 2017). Mesh resolution is prescribed by user-defined mesh-spacing functions. Ocean modeling focuses on resolving complicated shoreline boundaries, eddy activity, circulation pathways, computational constraints, and so on (Chassignet and Xu, 2021; Chen et al., 2003; Sein et al., 2017). To address this, several meshing tools have been developed. For example, Lambrechts et al. (2008) presented an unstructured spherical triangulation framework using the general-purpose grid generation package Gmsh. The OceanMesh2D tool builds coastal triangular meshes with an advancing-front method (Roberts et al., 2019), building on many of the ideas described in ADMESH (Conroy et al., 2012). Multi-scale land-surface modeling emphasizes faithfully reflecting the complex distribution of land cover and topography (Marsh et al., 2020). Marsh et al. (2018) presented multi-objective unstructured mesh generation software that constrains mesh generation to an arbitrary number of important features while maintaining a

https://doi.org/10.5194/egusphere-2026-6875
Preprint. Discussion started: 19 November 2026
© Author(s) 2026. CC BY 4.0 License.

variable spatial resolution. The LandMesh tool creates multi-scale hexagonal meshes for land-surface modeling and assigns resolution based on elevation, slope, land cover, and land use (Fan et al., 2024). These tools normally stop at mesh generation. Users still need solver-specific scripts to prepare model input files, which weakens reproducibility and makes cross-component studies harder to maintain. Furthermore, the applicability of a single grid generation tool across model components has yet to be systematically assessed.

This study investigates whether a single variable-resolution framework can adequately support atmospheric, oceanic, and land-surface models while maintaining the local accuracy of fine, uniform grids in regions of interest or throughout the Earth system modeling process. We develop EarthMesh, an automated tool for generating variable-resolution triangular meshes and their dual polygonal meshes on the sphere. EarthMesh selects cells for refinement from user-defined regions, from physical criteria such as LAI variability and land-cover diversity, or from a combination of both. Conforming transition rows with a user-specified width connect each refined region to the surrounding coarse mesh. A modified spring-dynamics optimization then reduces obtuse triangles in these transition zones by letting the equilibrium edge length follow the local refinement level. Model-specific drivers write input files for the Model for Prediction Across Scales-Atmosphere (MPAS-A), the Finite-Volume Community Ocean Model (FVCOM), and the Common Land Model Version 2024 (CoLM2024). We demonstrate the workflow with idealized atmospheric and oceanic tests and a realistic land-surface experiment. These tests also examine how the transition width, and the refinement criteria affect the simulation results.

2 EarthMesh workflow

EarthMesh generates meshes in four stages, which are shown in **Figure 1** and described below. It is noted that quasi-uniform meshes use only Stages A and D.

A. Initial construction

Construction of EarthMesh's unstructured grid begins with the generation of a

https://doi.org/10.5194/egusphere-2026-6875
Preprint. Discussion started: 19 November 2026
© Author(s) 2026. CC BY 4.0 License.

quasi-uniform global triangular (Delaunay) mesh. EarthMesh first projects a regular icosahedron onto the Earth's surface. Two of the 12 vertices are placed at the geographic poles, and the remaining vertices lie at latitudes arctan (±1/2). Each of the initial 20 spherical triangles is subdivided into NXP × NXP smaller triangles. Because EarthMesh subdivides the icosahedron non-recursively, NXP can be any positive integer, and NXP therefore also serves as the resolution parameter. For example, NXP = 64 gives an average horizontal spacing of about 120 km, while NXP = 768 indicates the average horizontal spacing of about 10 km. The spherical projection distorts the triangular cells, with stronger deformation as NXP increases (Walko and Avissar, 2008). The initial 120 km (NXP64) mesh before spring adjustment produced an interior-angle distribution ranging from 45° to 72°. As the grid resolution increased to 10 km (NXP768), the initial interior angle distribution widened, ranging from 35° to 75° (**Figure S1**). Previous studies have confirmed that the distorted triangular cells have a negative impact on the stability of numerical calculations (Iga and Tomita, 2014; Wang and Lee, 2011). To tackle this challenge, we adopt the spring-dynamics scheme of Tomita et al. (2002), treating each edge as a spring whose attraction or repulsion is determined by the difference between its current length and its equilibrium length. The default equilibrium length is the averaged distance between neighboring grids. This adjustment narrows the interior-angle distribution, Although the adjusted angular range widens with increasing resolution (Tomita et al., 2002), the distribution remains bounded within a narrow range across all tested resolutions (**Figure S1**, **Table S1**). In the 120 km mesh (NXP64), the distribution is bimodal, and all angles fall between approximately 53° and 72°. As resolution increases toward 10 km (NXP768), the distribution changes from bimodal to trimodal. The angular range stabilizes between approximately 47° and 72°. These results show that the icosahedral subdivision followed by global spring adjustment preserves near-equilateral triangular geometry over a wide range of mesh resolutions. The quasi-uniform meshes therefore provide a stable baseline for assessing the additional geometric effects introduced by local refinement.

B. Local refinement

Steps B1 to B3 form the refinement and connectivity reconstruction procedure.

https://doi.org/10.5194/egusphere-2026-6875
Preprint. Discussion started: 19 November 2026
© Author(s) 2026. CC BY 4.0 License.

Each pass through Stage B halves the local grid spacing, and the number of passes defines the refinement level (R). The area to be refined cannot cross the boundary of a previously refined area, since Stage B may be repeated to create multiple refinement levels.

B1: Selection and subdivision of refinement areas. EarthMesh offers two refinement modes (user-defined and adaptive, i.e., threshold-based) that can be used separately or together. The user-defined mode allows the user to specify one or more contiguous geographic regions for refinement. Selection criteria may include user interest and/or numerical solution requirements. There are no restrictions on the size or shape of the refinement area. For instance, users can select a refinement region using a refinement center plus influence radii, or use closed latitude-longitude polygons. The adaptive mode determines the refinement areas based on various metrics, such as the standard deviation of LAI or the number of land-cover types per cell. Each triangle with at least one vertex inside the selected area is subdivided into four triangles by connecting the midpoints of its edges.

B2: Expansion of the refined area. EarthMesh expands the refined regions when needed so that vertices in the transition rows constructed in step B3 have valence 5, 6, or 7 (Walko and Avissar, 2011). We define a sharp exterior concavity as a vertex point along the perimeter of a refined area for which exactly one triangle containing it is unrefined, and a weak concavity as a vertex point where exactly two (adjacent) triangles are unrefined. The expansion procedure first eliminates sharp concavities, and then merges any two refined regions that are separated by fewer than $2M$ cell rows, where M is the number of transition rows. Since the step B2 retains weak concavities along the refinement boundary, it accommodates a much wider range of shapes of the refined region.

B3: Elimination of hanging nodes. The nodes generated at the edges of the original triangle during mesh refinement are referred to as “hanging nodes”, as can be seen in **Figures S2a and S3a**. These nodes break mesh conformity because a conforming triangular mesh requires each cell to share full-length edges with its three neighbors. The simplest elimination approach is presented in (Fan et al., 2024; Logemann et al.,

https://doi.org/10.5194/egusphere-2026-6875
Preprint. Discussion started: 19 November 2026
© Author(s) 2026. CC BY 4.0 License.

2021), and consists of adding one edge for each hanging node, connecting it with the opposite vertex of the adjacent unrefined triangle. EarthMesh removes hanging nodes outside the refined area and controls the resolution gradation across the refinement boundary by reconstructing connectivity through one or more transition rows (M). Simultaneously, EarthMesh enforces a constraint that the deviation of each vertex's 6 edges does not exceed ± 1. These methods aim to avoid a decrease in numerical accuracy due to some adjacent triangles deviating from the quasi-equilateral shape. Two reconstruction strategies are discussed in the following, depending on whether weak concavities along the refined boundary.

Figure S2 illustrates the reconstruction in a refinement region without weak concavities using $M = 4$. Each set of M adjacent hanging nodes forms a triangular color group. Reconstruction then proceeds through at most M loops. Each loop applies three local operations (ODT, ODTR, and LOP) within the group, involving both adding new edges and removing old ones. The ODT operation adds one edge per hanging node, connecting the node to the opposite vertex of the adjacent unrefined triangle, thereby splitting one triangle into two (**Figure S2**, left column). The ODTR operation reverses that split in adjacent unrefined triangles by adding edges to unrefined triangles adjacent to those modified by ODT (**Figure S2**, middle column). The LOP operation swaps diagonals in convex quadrilaterals, thereby replacing old edges with new edges aligned with the adjacent group boundary (**Figure S2**, right column). After each loop, the hanging nodes move outward from the refinement boundary, and the number of hanging nodes decreases by 1. It is generally impossible to exactly fill the refined boundary with the same M construction without leaving a remainder. Any remaining length can be filled with the smaller M ($M = 1$, 2, or 3). When constructions of different sizes coexist along the refined-grid perimeter, M is defined as the largest construction present.

where weak concavities exist along the refined boundary, as seen in the **Figure S3**, two adjacent triangular color groups merge into a quadrilateral group. The reconstruction still uses ODT, ODTR, and LOP. In this case, LOP also removes the central axis of the weak-concavity region so that vertex valence remains between 5 and 7 (**Figure S3**, right column).

https://doi.org/10.5194/egusphere-2026-6875
Preprint. Discussion started: 19 November 2026
© Author(s) 2026. CC BY 4.0 License.

C. Mesh optimization

Transition rows preserve mesh conformity but inevitably create obtuse triangles at boundary vertices that contain five edges (Logemann et al., 2021). Such obtuse triangles can degrade numerical stability and are incompatible with models using C-grid numerical calculation methods (Ringler et al., 2013; Skamarock et al., 2012). To mitigate this issue, EarthMesh applies a modified spring-dynamics optimization that adjusts the equilibrium spring length based on the local refinement level. Specifically, the equilibrium length halves within each refinement region but varies linearly across the transition zone (**Figure S4**, red lines). A uniform equilibrium length, as in the original scheme of Tomita et al. (2002), would pull the refined cells back toward the coarse spacing and erode the refinement; scaling the equilibrium length with the local refinement level preserves the target resolution while relaxing the cell shapes. Taking a 30-120 km variable-resolution atmospheric grid as an example, the equilibrium length of the initial grid is 120 km, while the first refinement level reduces to 60 km. In the transition area of the first-level refinement region, the equilibrium length varies linearly from 60 km to 120 km, and so forth. We construct atmospheric variable-resolution grids with different M, and examine the impact of M on grid quality. The initial 30–120 km mesh yields interior angles ranging from 26.39° to 124.76°. The modified adjustment scheme substantially improves grid quality. The interior-angle distribution of atmospheric mesh with a single transition row narrowed to 29.00° - 90.15°. As M increases to 4, the interior-angle distribution narrows further to 36.52° - 86.07° (**Table S2**). Similar behavior is found for the 10–40 km variable-resolution oceanic grids, whose results are reported in **Table S3**.

D. Output generation

EarthMesh can output triangular meshes or dual-polygonal meshes. For triangular output, the optimized mesh from Stage C is written directly. For polygonal output, EarthMesh connects either the circumcenters or the centroids of adjacent triangle pairs. The circumcenter method produces Voronoi diagrams that satisfy local orthogonal staggering when all triangular cells have interior angles below 90°, making this output suitable for C-grid atmospheric models such as MPAS-A. The centroid method keeps

https://doi.org/10.5194/egusphere-2026-6875
Preprint. Discussion started: 19 November 2026
© Author(s) 2026. CC BY 4.0 License.

each polygon's center within its parent triangle and prevents partial overlaps or gaps between neighboring polygons, even when obtuse triangles remain. This output is suitable for column-based land-surface models such as CoLM2024. EarthMesh includes output drivers that generate the required input files for MPAS-A, FVCOM, and CoLM2024.

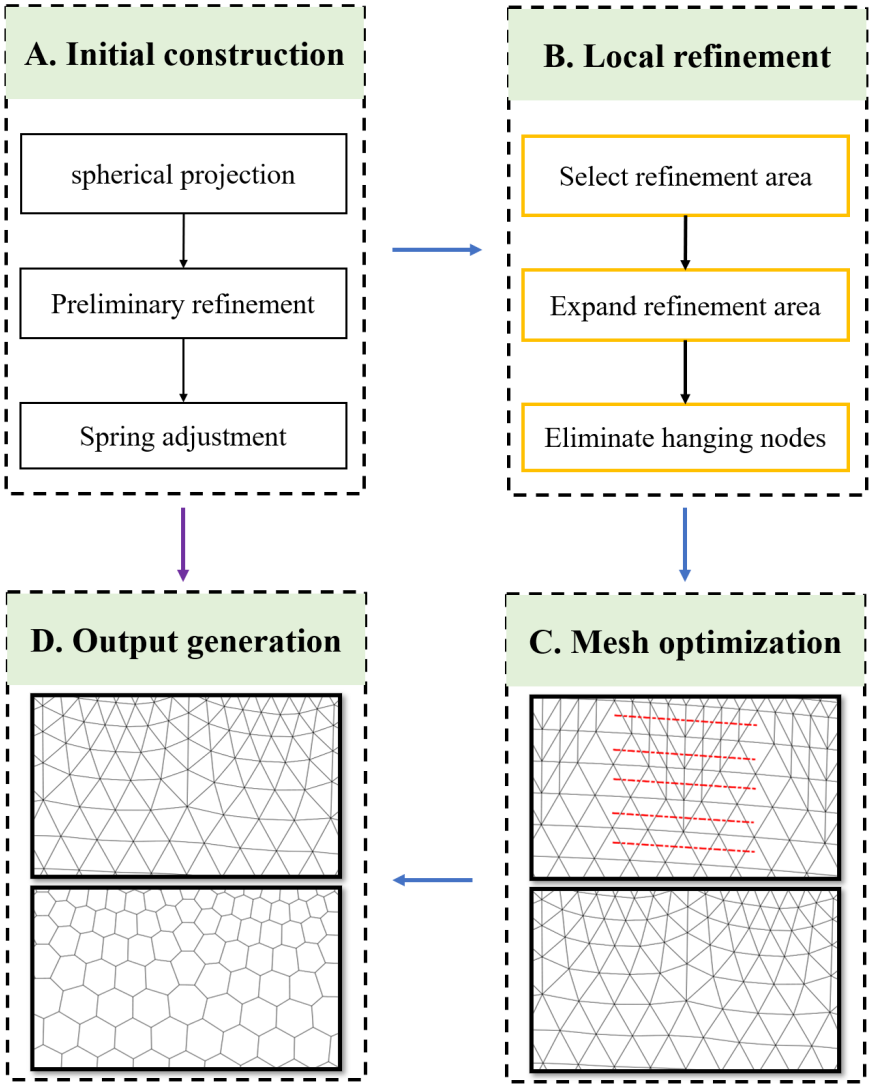


Figure 1. The workflow of unstructured mesh generation in EarthMesh. The workflow includes four major components: initial mesh construction, local mesh refinement, mesh quality optimization, and

https://doi.org/10.5194/egusphere-2026-6875
Preprint. Discussion started: 19 November 2026
© Author(s) 2026. CC BY 4.0 License.

output generation. The yellow boxes highlight the steps that may be run recursively. The purple and blue arrows represent the generation processes of the quasi-uniform and variable-resolution grids, respectively.

3 Methods

3.1 Model integration and grid requirements

MPAS-A solves the fully compressible non-hydrostatic atmosphere equations on a C-grid staggered unstructured Voronoi mesh (Skamarock et al., 2012). Spherical centroidal Voronoi tessellations allow the same solver to run on quasi-uniform meshes or on meshes with smoothly varying resolution (Ringler et al., 2011). This mesh flexibility enables global, uniform-resolution numerical weather prediction and climate simulations, as well as regional high-resolution applications. MPAS-A uses a geometric-height hybrid terrain-following vertical coordinate (Klemp, 2011). Time integration uses a third-order Runge-Kutta scheme with explicit time splitting (Wicker and Skamarock, 2002).

FVCOM solves free-surface, three-dimensional primitive equations on an unstructured triangular B-grid with a finite-volume formulation (Chen et al., 2003). The model uses a terrain-following sigma coordinate vertically and non-overlapping triangular cells horizontally. Unstructured triangular meshes represent estuaries and coastlines without the stair-step errors common in structured grids (Chen et al., 2007). Time integration uses a modified fourth-order Runge-Kutta time-stepping scheme, with shorter steps for the barotropic mode and longer steps for the baroclinic modes.

CoLM2024 is a column-based land-surface model with land-cover options from the International Geosphere-Biosphere Program (IGBP; Loveland et al., 2000) and the United States Geological Survey (USGS). It can run on longitude-latitude grids, unstructured grids, and catchment-based grids (Dai et al., 2003; Fan et al., 2024; Huang et al., 2022). CoLM2024 uses a two-level spatial hierarchy. Fluxes of matter and energy between the atmosphere, vegetation, soil, and water surface are computed for each patch and then aggregated to the grid-cell level by patch fractional cover.

3.2 Experiment Design

https://doi.org/10.5194/egusphere-2026-6875
Preprint. Discussion started: 19 November 2026
© Author(s) 2026. CC BY 4.0 License.

We use three experiment sets to evaluate EarthMesh in atmospheric, oceanic, and land-surface applications. Both refinement modes are demonstrated, with user-defined refinement in the atmospheric and oceanic experiments and adaptive (threshold-based) refinement in the land-surface experiment. Our objective is to assess the impact of local mesh refinement, especially with different refinement configurations, on the solution accuracy compared with quasi-uniform meshes. Each experiment set includes a coarse uniform run (LR), a fine uniform run (HR), and a series of variable-resolution runs (VR). LR and HR serve as baselines to test whether VR can reproduce fine-scale features. In the experiment IDs, the prefix (A, O, or L) denotes the model component, R2 denotes two refinement levels (a factor-of-four reduction in grid spacing), and Mn denotes n transition rows. Mesh-generation parameters are listed in Tables 1–3, and full experimental details are given in **Text S1-S3**, respectively.

Table 1. Model configurations for the atmospheric experiment sets

ID	Rows	Res. (km)	Cells
A1	/	120	40,962
A2	/	30	655,362
A-R2M2	2	30-120	54,913
A-R2M3	3	30-120	54,330
A-R2M4	4	30-120	53,749

Table 2. Model configurations for the oceanic experiment sets

ID	Rows	Res. (km)	Cells
O1	/	40	5,535
O2	/	10	88,119
O-R2M1	1	10-40	41,238
O-R2M2	2	10-40	40,428
O-R2M3	3	10-40	39,407
O-R2M4	4	10-40	38,381

https://doi.org/10.5194/egusphere-2026-6875
Preprint. Discussion started: 19 November 2026
© Author(s) 2026. CC BY 4.0 License.

Table 3. Model configurations for the land surface experiment sets. LAI_{std}: LAI standard deviation; $N_{landtypes}$: The number of land types

ID	Threshold	Res. (km)	Cells
L1	/	53.3	1,375
L2	/	13.3	21,317
L-lai-1	$LAI_{std} > 1.2$	13.3-53.3	13,560
L-lai-2	$LAI_{std} > 1.6$	13.3-53.3	5,414
L-lai-3	$LAI_{std} > 2.0$	13.3-53.3	1,572
L-landtypes-1	$N_{landtypes} > 8$	13.3-53.3	5,631
L-landtypes-2	$N_{landtypes} > 9$	13.3-53.3	2,855
L-landtypes-3	$N_{landtypes} > 10$	13.3-53.3	1,584
L-lai-landtypes	$LAI_{std} > 1.6$; $N_{landtypes} > 10$	13.3-53.3	6,035

The atmospheric experiments use MPAS-A to conduct the Jablonowski-Williamson baroclinic wave test on a global scale (Jablonowski and Williamson, 2006). The two global quasi-uniform meshes are A1 at 120 km (LR) and A2 at 30 km (HR). The VR meshes are refined within a 2,000 km radius centered at 40°N, 120°E, so that the developing baroclinic wave crosses the transition zone during the integration (**Figure 2, Table 1**). This design follows earlier MPAS-A evaluations of the same test case on variable-resolution meshes (Park et al., 2013). Thus, the results can be compared with published solutions. The aim of this evaluation is to examine the impact of the chosen *M* that span the resolution transition zone. Note that the mesh with a single transition row is not tested because it does not meet the C-grid constraint of MPAS-A (**Table S2**). We evaluate model performance by comparing surface pressure and 850 hPa relative vorticities against the quasi-uniform runs, focusing on whether a variable-resolution mesh can reproduce the baroclinic wave evolution obtained from a uniform high-resolution mesh while avoiding artifacts at the refinement boundary.

The oceanic experiments use FVCOM over the coastal seas of China (12-42°N,

https://doi.org/10.5194/egusphere-2026-6875
Preprint. Discussion started: 19 November 2026
© Author(s) 2026. CC BY 4.0 License.

105-135°E) with an idealized geostrophic eddy test. The two quasi-uniform meshes are O1 at 40 km (LR) and O2 at 10 km (HR). The VR meshes place 10 km cells along coastal zones and gradually coarsen to 40 km offshore, created to investigate coastal processes at high resolution while avoiding the cost of high-resolution running over the whole domain (Hoch et al., 2020; Logemann et al., 2021). Four VR meshes are designed to evaluate the impact of *M* across the resolution transition zone (**Figure 3, Table 2**). We compare velocity fields to assess how local resolution affects eddy structure and the ability to maintain velocity extrema.

The land-surface experiments use CoLM2024 over the eastern United States (25-50°N, 95-65°W). The two quasi-uniform meshes are L1 at 53.3 km (LR) and L2 at 13.3 km (HR). Because multi-scale land-surface modeling needs to represent the complex distribution of land cover and topography (Marsh et al., 2018, 2020), a practical question is how to vary the resolution and where to deploy the refinement (Fan et al., 2024). We show an example of adaptive refinement that selects cells based on LAI heterogeneity and/or the number of land-cover types within each cell. Compared with user-defined refinement, it has greater flexibility in determining refinement areas. To quantify the impact of threshold parameter values and threshold numbers on grid resolution deployment, a series of VR meshes are configured and the relevant parameters are shown (**Figure 4, Table 3**). A relatively small threshold may lead to insufficient mesh refinement, while an excessively large threshold may result in a larger refinement region, or even close to global refinement. With an automated tool, users can revise the refinement configuration and regenerate the mesh until it meets their needs. The land surface variable-resolution experiment uses the mesh presented in **Figure 4b**. These experiments evaluate whether local refinement improves runoff simulation relative to the coarse baseline.

https://doi.org/10.5194/egusphere-2026-6875
Preprint. Discussion started: 19 November 2026
© Author(s) 2026. CC BY 4.0 License.

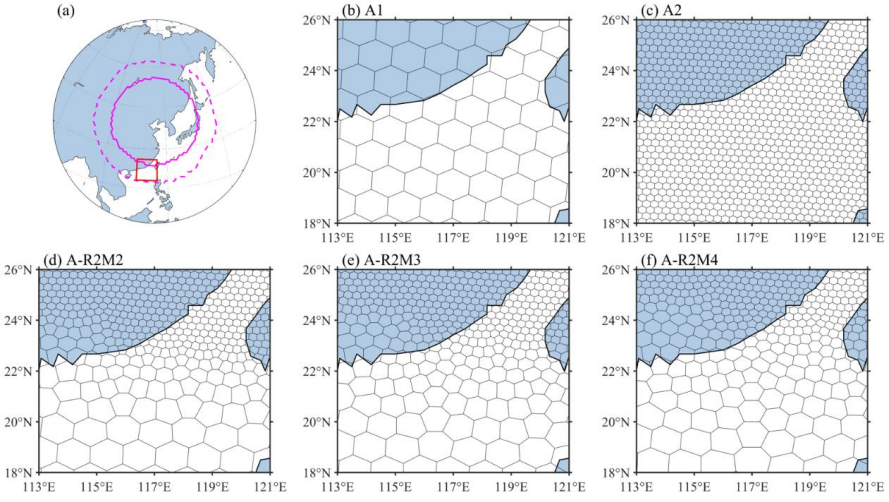


Figure 2. The geographical location and grids of the atmospheric cases used as examples in this work. The purple lines represent the resolution boundaries: 120 km (dashed) and 30 km (solid) in (a). The grid details in red boxes of (a) are shown in (b-f), respectively.

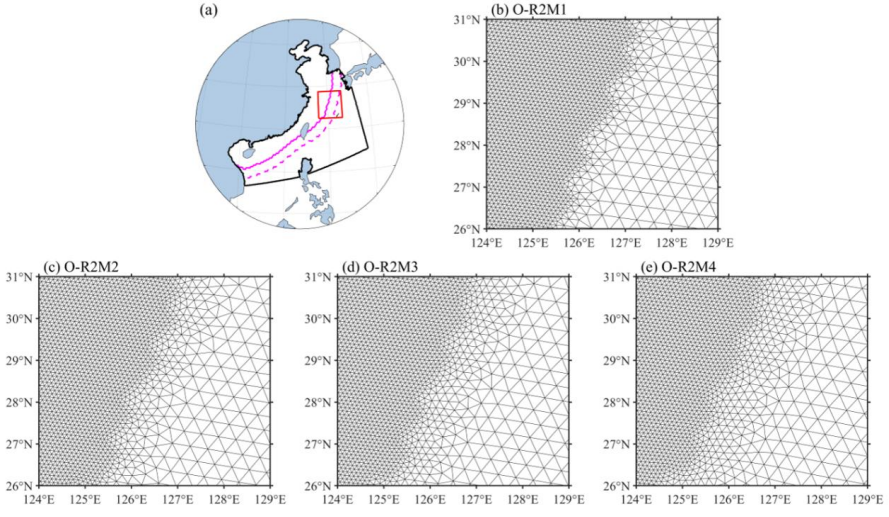


Figure 3. The geographical location and grids of the oceanic cases used as examples in this work. The purple lines represent the resolution boundaries: 40 km (dashed) and 10 km (solid) in (a). The black closed curves in (a) represent the boundaries of simulation area. The grid details in red boxes of (a) are shown in (b-e), respectively.

https://doi.org/10.5194/egusphere-2026-6875
Preprint. Discussion started: 19 November 2026
© Author(s) 2026. CC BY 4.0 License.

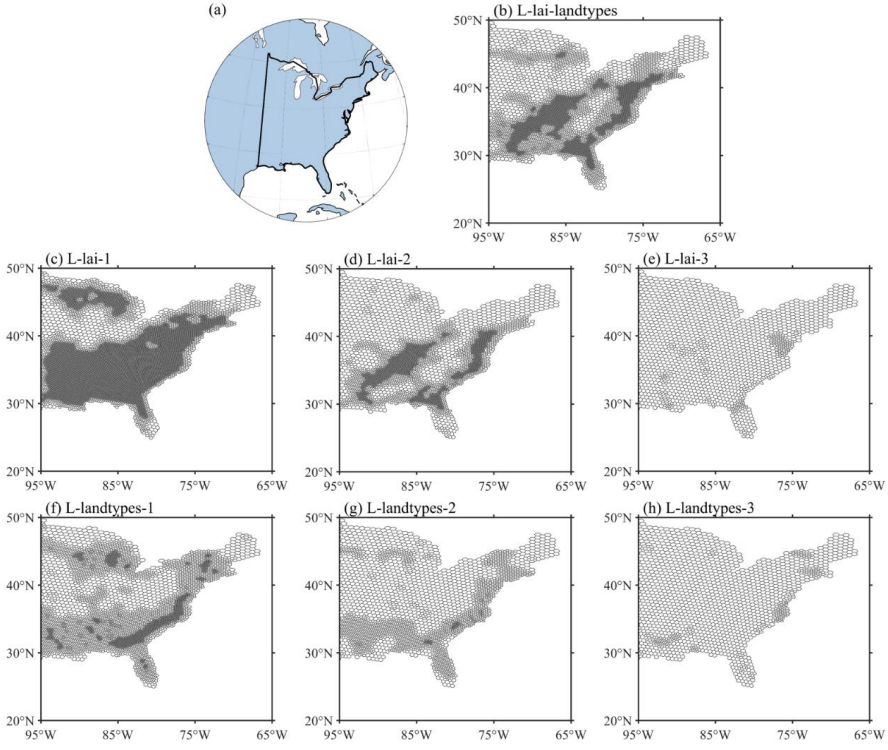


Figure 4. The geographical location and grids of the land surface cases used as examples in this work. The black closed curves in (a) represent the boundaries of simulation area. The grid details within the black closed curves are shown in (b-h), respectively.

4 Results

4.1 Atmospheric simulation

The results of two quasi-uniform meshes (see **Table 1,** A1 and A2) are summarized in **Figure 5**, showing the surface pressure and 850 hPa relative vorticity after 7 days of simulation. Although both experiments capture the large-scale twin-cyclone structure, the coarse, uniform A1run underestimates the intensity of the developing disturbance. Specifically, its baroclinic wave train exhibits a phase lag, and the central pressure of the two main cyclones is higher than in the reference A2 run, consistent with previous studies (Skamarock et al., 2012; Zängl et al., 2022).

We next introduce local mesh refinement over a roughly circular region. For the first refined experiment (see **Table 1,** A-R2M2), we set $M = 2$, so that each doubling of

https://doi.org/10.5194/egusphere-2026-6875
Preprint. Discussion started: 19 November 2026
© Author(s) 2026. CC BY 4.0 License.

resolution occurs abruptly across two transition rows of grid cells. The experiment reproduces the main features of A2 within the refined region. The locations of the low-pressure centers, the shape of the surface pressure contours, and the distribution of 850 hPa relative vorticity closely follow the high-resolution reference (**Figure 6, top row**). The results indicate that even with M = 2, both the surface pressure field and the vorticity field change smoothly across the boundary between the 30 km and 120 km regions. The fields do not exhibit artificial discontinuities, isolated extrema, or reflected-wave patterns along the transition line. These results agree with Park et al. (2013), who found no apparent wave distortion in the fine-to-coarse transition region of MPAS-A variable-resolution meshes. We repeat the baroclinic wave test with M = 3 and 4 and also show the results in the second and third rows of **Figure 6**. Increasing M to makes the transition between the fine and coarse regions more gradual and better preserves the fine baroclinic-wave structure. These benefits make the simulation of the downstream coarse resolution regions closer to reference simulation.

Figure 7 shows a quantitative comparison for the first 12 model days, as the spread of the numerical solutions increases noticeably thereafter (Jablonowski and Williamson, 2006). The regional Root Mean Square Error (RMSE) of each test is computed over 10–70°N, 70°E–150°W against the highest resolution (A2). Three VR meshes (A-R2M2, A-R2M3, and A-R2M4) exhibit larger errors overall than A1 mesh during the first 6 model day. As noted by Zhou et al. (2020), the initial phase of the baroclinic wave growth (0-6 days) is easily dominated by interpolation errors. Slightly smaller errors were observed in the three VR meshes compared to the A1 mesh from day 7 to day 12. These results suggest that the VR meshes can improve the accuracy of local simulation, while solution error is controlled primarily by the grid resolution in the coarsest part of the model domain, reconfirming the conclusion of Ringler et al. (2011).

https://doi.org/10.5194/egusphere-2026-6875
Preprint. Discussion started: 19 November 2026
© Author(s) 2026. CC BY 4.0 License.

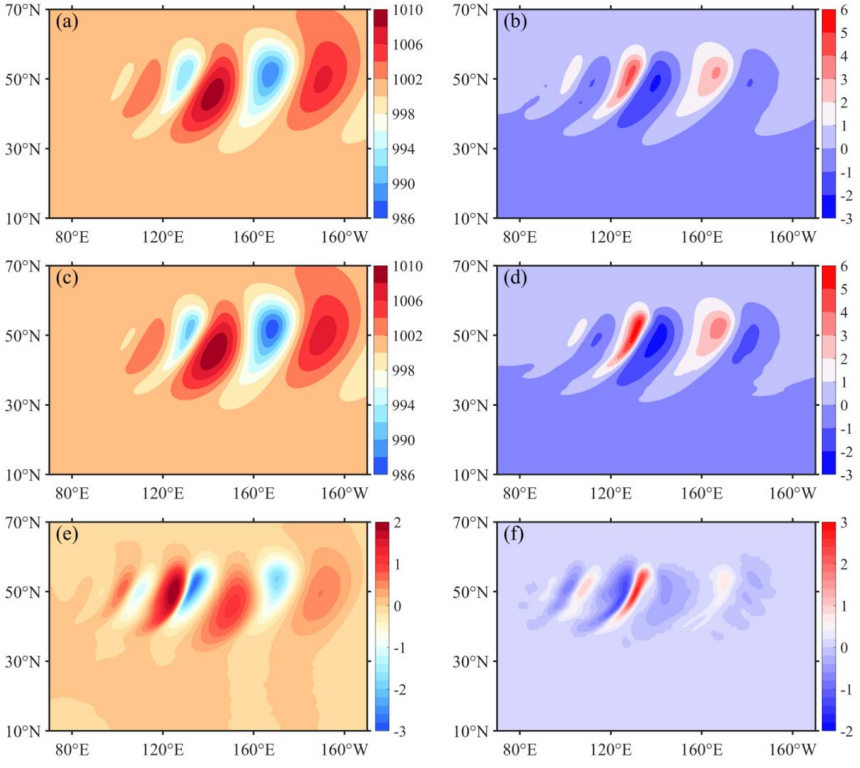


Figure 5. Surface pressure (hPa, left column) and 850 hPa relative vorticity (10^{-5} s^{-1}, right column) for experiments A1 (a, b), A2 (c, d), and their difference (e, f) after 7 model days.

https://doi.org/10.5194/egusphere-2026-6875
Preprint. Discussion started: 19 November 2026
© Author(s) 2026. CC BY 4.0 License.

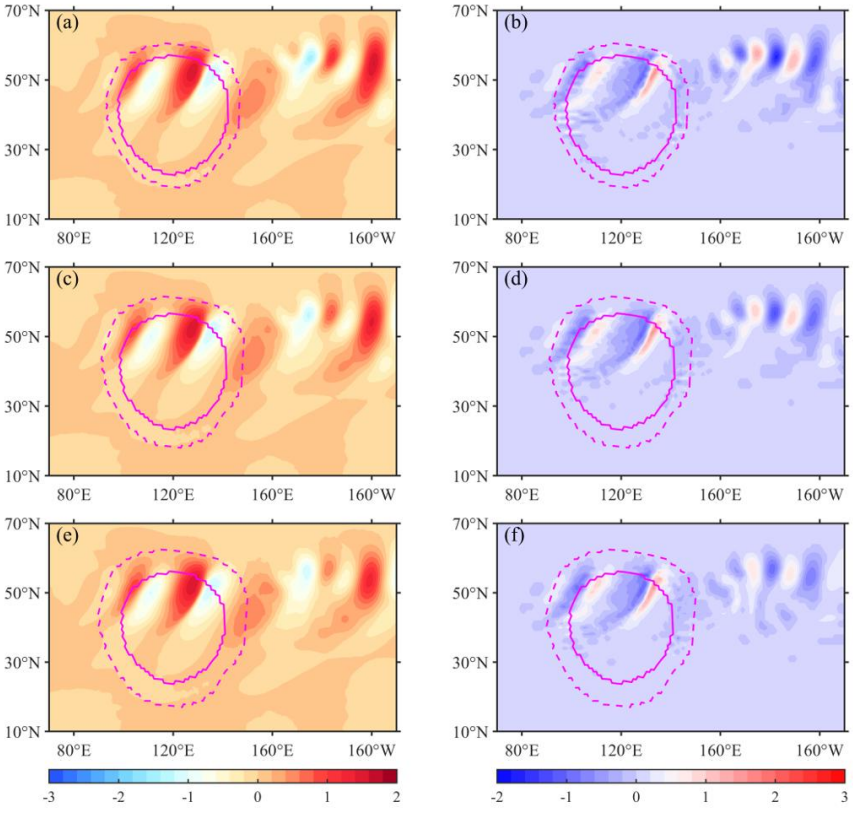


Figure 6. The differences in surface pressure (hPa, left column) and 850 hPa relative vorticity (10^{-5} s^{-1}, right column) for experiments A-R2M2 (a, b), A-R2M3 (c, d), A-R2M4 (e, f) compared with experiment A2 after 7 model days. Purple solid and dashed lines mark the approximate 30 km and 120 km mesh-spacing boundaries, respectively.

https://doi.org/10.5194/egusphere-2026-6875
Preprint. Discussion started: 19 November 2026
© Author(s) 2026. CC BY 4.0 License.

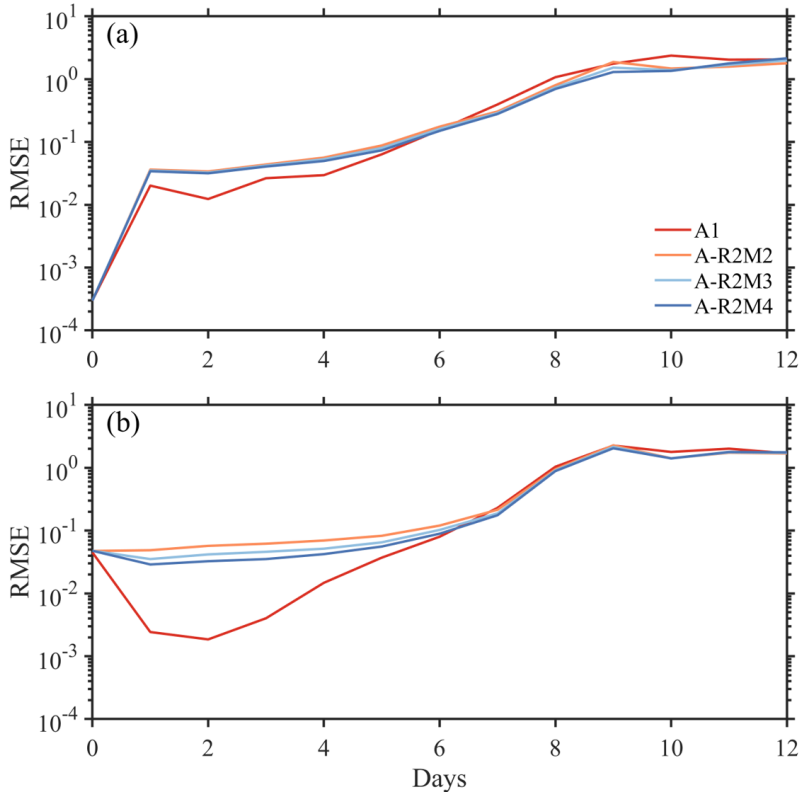


Figure 7. The Root Mean Square Error (RMSE) of surface pressure (hPa, left) and 850 hPa relative vorticity (10^{-5} s^{-1}, right) as a function of time. The error is computed against the high-resolution quasi-uniform A1 mesh.

4.2 Ocean simulation

Figure 8 shows the eastward and northward velocities of the two quasi-uniform meshes after 10 model days of integration. Although the coarse mesh O1, with a nominal resolution of 40 km, maintains the basic structure of the large-scale geostrophic flow, its maximum velocity is only 0.36 m s^{-1}, noticeably lower than the 0.46 m s^{-1} produced by the high-resolution experiment O2, and its velocity field exhibits visibly jagged structures. This indicates that the coarse grid, being unable to resolve the radial and azimuthal gradients near the eddy, causes the velocity field to be over-smoothed, thereby weakening its ability to maintain velocity extrema.

Compared with O1, O-R2M1 shows smaller and less widespread differences from

https://doi.org/10.5194/egusphere-2026-6875
Preprint. Discussion started: 19 November 2026
© Author(s) 2026. CC BY 4.0 License.

O2 with maximum velocity of, indicating that it is closer overall to the high-resolution reference solution (**Figure 9 and S6, Table 2**). The variable-resolution experiments also indicate that the velocity field structure is highly sensitive to the local grid resolution, i.e., finer flow structures appear in the refined region, whereas coarser structures appear in the coarse region. Even in the coarse-resolution coverage area, the variable-resolution simulation can maintain the velocity extrema of the geostrophic flow better than the purely coarse-mesh experiment. This is likely due to the eddy structure resolved in the refined region is carried through the transition zone into the coarse region, where it decays more slowly than an eddy generated on a uniformly coarse mesh (Danilov and Wang, 2015; Hoch et al., 2020). Increasing *M* helps further reduce the difference from the high-resolution simulation, making the velocity field smoother and the errors smaller (**Figure 9 and S6**). This reduction in error is further quantified by the time series of RMSE relative to the high-resolution simulation (**Figure 10**). The separation among the RMSE curves is established early in the integration and persists over time, indicating that the improvement is not a transient effect. However, this benefit is nonlinear. Once the number of transition rows exceeds 2, further increases yield only limited error reduction. For FVCOM, a setting of two transition rows may already be sufficient, as it achieves a good balance between computational cost and simulation accuracy.

https://doi.org/10.5194/egusphere-2026-6875
Preprint. Discussion started: 19 November 2026
© Author(s) 2026. CC BY 4.0 License.

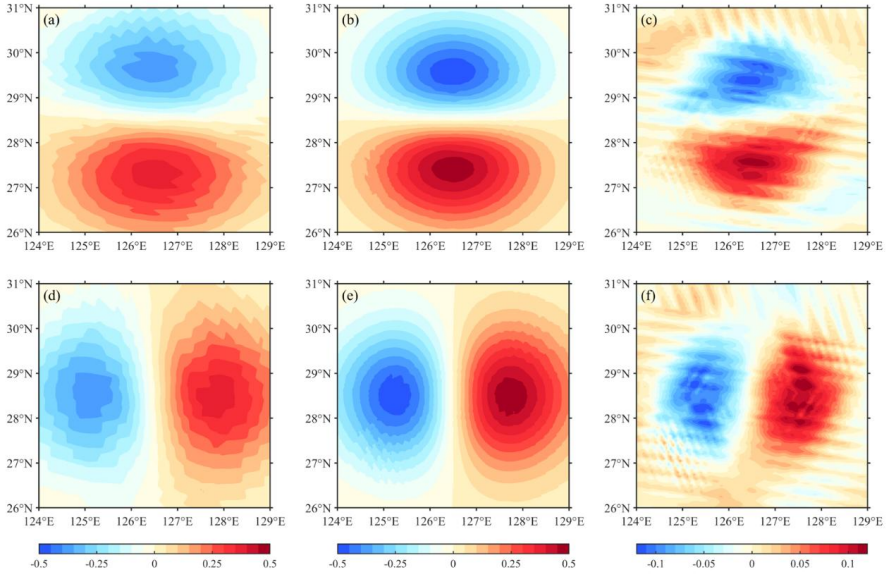


Figure 8. Eastward surface velocity (m s^{-1}), and northward surface velocity (m s^{-1}) for experiments O1 (a, d), O2 (b, e), and their difference (O2 - O1) (c, f) after 10 model days.

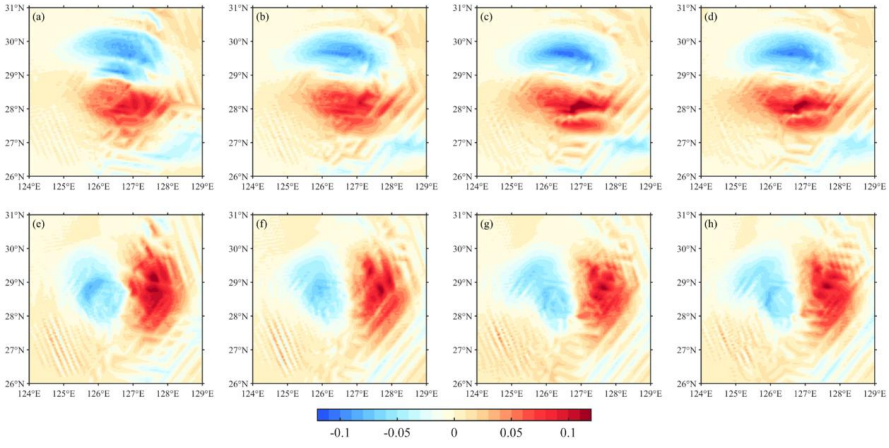


Figure 9. The differences in eastward surface velocity (m s^{-1}, top row) and northward surface velocity (m s^{-1}, second row) for experiments O-R2M1 (a, e), O-R2M2 (b, f), O-R2M3 (c, g), O-R2M4 (d, h) compared with experiment O2 after 10 model days.

https://doi.org/10.5194/egusphere-2026-6875
Preprint. Discussion started: 19 November 2026
© Author(s) 2026. CC BY 4.0 License.

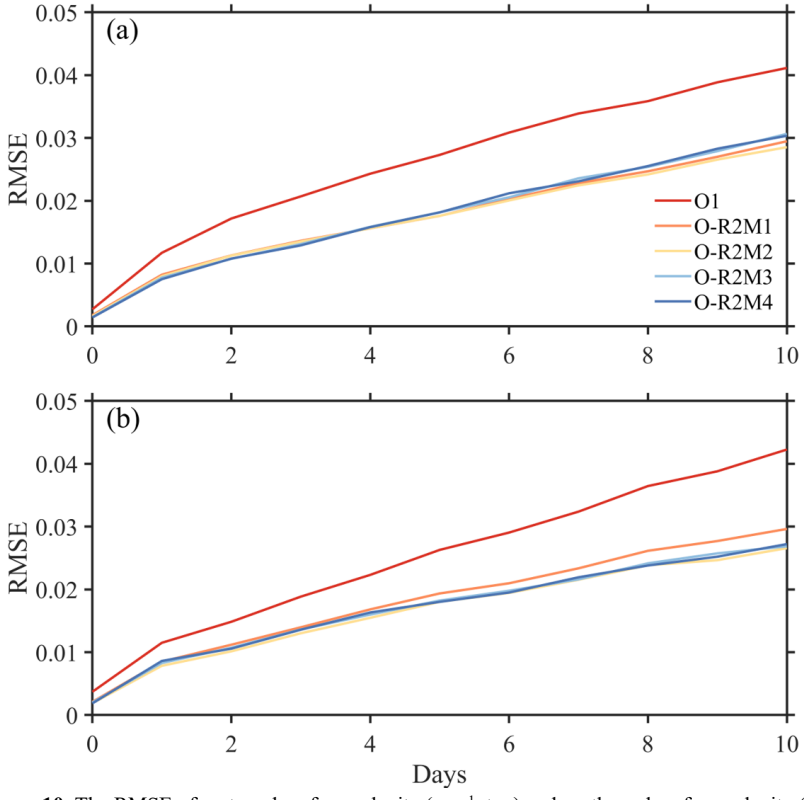


Figure 10. The RMSE of eastward surface velocity (m s^{-1}, top) and northward surface velocity (m s^{-1}, bottom) as a function of time. The error is computed against the high-resolution quasi-uniform O2 mesh.

4.3 Land-surface simulation

Figure 11 compares Kling-Gupta Efficiency Skill Score (KGESS, Knoben et al., 2019) values against the GRFR runoff dataset (Yang et al., 2021) for the 2006 to 2010 analysis period. The coarse-resolution experiment L1 produces a domain-mean KGESS of 0.45, and KGESS exceeds 0.2 over most of the domain (**Figure 11d**). The model performs reasonably well over relatively homogeneous regions, such as parts of the Great Plains, but its skill decreases over the Appalachian region and other areas with more pronounced terrain and land-cover heterogeneity (**Figure 11a**). This spatial pattern indicates that the 53.3 km mesh smooths surface characteristics that affect runoff generation and routing at smaller scales. The uniform high-resolution experiment L2 increases the nominal resolution to 13.3 km, and yields the same domain-mean

https://doi.org/10.5194/egusphere-2026-6875
Preprint. Discussion started: 19 November 2026
© Author(s) 2026. CC BY 4.0 License.

KGESS value (0.45), indicating that their gains are spatially redistributed. It does not improve runoff skill everywhere relative to L1; KGESS increases over approximately 62% of the domain. The gains are concentrated in areas where the coarse grid underrepresents spatial variability in vegetation, land cover, and topography (**Figure 11b**). The improved spatial pattern suggests that finer land-surface discretization can better preserve subregional heterogeneity relevant to runoff simulation, but it also highlights that identifying where enhanced resolution is required is equally important.

The adaptive variable-resolution experiment L-lai-landtypes also produces a domain-mean KGESS of 0.45, with a similar but slightly weaker improvement pattern as the experiment L2. KGESS increases across approximately 55% of the domain relative to L1. Areas selected for refinement based on LAI variability and land-cover diversity show improvements comparable to those in L2, while more homogeneous areas remain close to the coarse-resolution result. This behavior matches the design of the adaptive refinement scheme. It adds resolution where surface heterogeneity is high and avoids unnecessary refinement where the coarse grid already represents dominant land-surface properties.

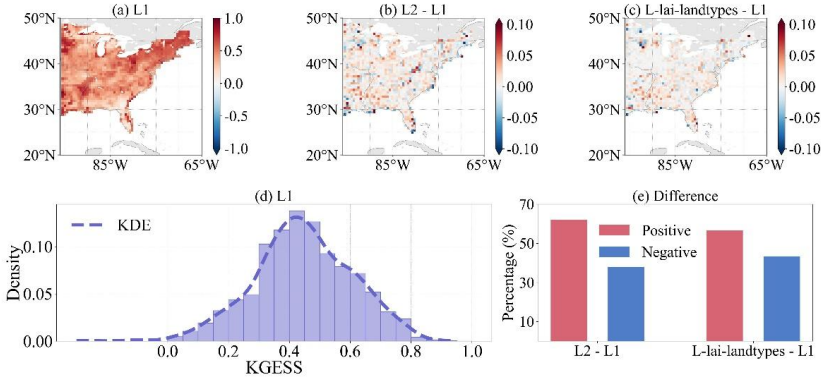


Figure 11. KGESS values from the low-resolution simulation (a), KGESS differences between the low-resolution and high-resolution simulations (b), and KGESS differences between the low-resolution and variable-resolution simulations (c) at the monthly time scale. Panels (d) and (e) show the kernel-density distribution from the low-resolution simulation and the difference statistics, respectively. Positive KGESS indicates acceptable model performance. Validation uses the Global Reach-level Flood Reanalysis (GRFR) dataset.

https://doi.org/10.5194/egusphere-2026-6875
Preprint. Discussion started: 19 November 2026
© Author(s) 2026. CC BY 4.0 License.

5 Discussion

5.1 Performance of variable-resolution meshes across model components

The three experiments show that a single meshing framework can support atmospheric, oceanic, and land-surface applications, although these components differ in equations, numerical discretization, and mesh requirements. This transferability comes from separating the meshing problem into two linked decisions, i.e., where fine resolution is needed, and how the refined region connects to the surrounding coarse mesh without creating poor-quality elements at the boundary. EarthMesh treats these decisions separately. Refinement can be prescribed by the user, derived from physical heterogeneity, or combined across criteria, while transition-zone construction and spring adjustment are applied after the refinement region has been selected.

The atmospheric and oceanic tests provide a direct check on the effect of the multi-row transition construction and spring adjustment scheme. In atmospheric variable-resolution tests, the baroclinic wave crosses the boundary between the 30 km and 120 km regions without visible pressure discontinuities or reflected vorticity structures. In oceanic variable-resolution tests, the velocity fields remain smooth as the mesh transitions from 10 km coastal resolution to 40 km offshore resolution. This behavior agrees with Park et al. (2013), who found no apparent wave distortion in the fine-to-coarse transition region of MPAS variable-resolution meshes, and with the multiresolution shallow-water experiments of Ringler et al. (2011). The mesh-quality statistics show that the effect of the spring adjustment scheme varies with the construction method, the number of transition rows, and the size of the refinement area (**Tables S2 and S3**). After the spring adjustment, A-R2M4 angles fall between 36.52° and 86.07°, and O-R2M3 angles fall between 36.96° and 87.22°, removing the most distorted cells that appeared before the adjustment. Once the transition zone is well constructed, the benefit of geometric refinement is large relative to its cost. A-R2M2, for example, contains only about 34 % more cells than A1 (54,913 versus 40,962), yet it reproduces the A2 solution within the target region (**Figures 6 and 7**).

https://doi.org/10.5194/egusphere-2026-6875
Preprint. Discussion started: 19 November 2026
© Author(s) 2026. CC BY 4.0 License.

The land-surface test shows that what constitutes adequate mesh quality differs among model components, and suggests that for land-surface simulation, refinement guided by surface heterogeneity can be more efficient than uniform refinement (Marsh et al., 2018). For CoLM2024, the more relevant question is whether the mesh preserves surface heterogeneity that controls runoff generation. L-lai-landtypes uses physical refinement based on variability in LAI and land-cover diversity. Homogeneous plains retain coarse cells, whereas rugged or densely vegetated regions receive fine cells. L-lai-landtypes, therefore, retains much of the skill gain of L2 while using only 28.3% of its cells (**Table 3**). This contrast suggests that physically informed criteria can allocate resolution more efficiently than uniform refinement when relevant heterogeneity fields are available, although a geometric-refinement control with a similar cell count would be needed to confirm their advantage over user-defined regions (Marsh et al., 2020).

5.2 Implications for mesh design across atmosphere, ocean, and land models

The atmospheric experiment places the strongest constraint on mesh geometry. MPAS-A uses a C-grid finite-volume formulation on a Voronoi mesh, so the triangular primal mesh must support a well-behaved dual mesh (Jacobsen et al., 2013). This requirement emphasizes suppressing obtuse triangles and controlling the number of edges meeting at each vertex (Walko and Avissar, 2011). A transition boundary with poorly shaped triangles would alter local orthogonality, distort flux operators, and possibly change the phase speed of propagating waves. The atmospheric results suggest that two transition rows are sufficient for this idealized baroclinic wave case, but this result should not be interpreted as a universal rule. A smaller refinement region, stronger flow gradients, or longer integration may require a different transition width.

The ocean experiment imposes a different constraint on mesh quality. FVCOM solves directly on triangular cells, so the primal mesh quality is exposed to the solver. The oceanic variable-resolution experiments show that coastal refinement can resolve the eddy-driven velocity structure in the fine-mesh region, while the coarser offshore region still captures the broader pressure response. The serrated velocity patterns in O1 and in the coarse part of the oceanic variable-resolution experiments indicate that local resolution controls the representation of eddy gradients. This result supports the idea

https://doi.org/10.5194/egusphere-2026-6875
Preprint. Discussion started: 19 November 2026
© Author(s) 2026. CC BY 4.0 License.

that variable-resolution ocean meshes should place refinement according to sea surface height variability (Sein et al., 2016), the local Rossby radius of deformation (Sein et al., 2017), velocity shear, or bathymetric complexity (Barton et al., 2022), rather than relying only on a fixed distance from the coast.

The land-surface experiment requires a different interpretation of the benefit of resolution. L2 and L-lai-landtypes improve runoff skill over many parts of the domain, but some cells show lower KGESS than in L1. This does not mean that the refined meshes failed. It shows that finer land grids can reveal mismatches between resolved surface properties and the model's forcing or physics. They can also reveal missing lateral redistribution processes in a column-based land model. Higher spatial resolution alone therefore cannot eliminate all sources of runoff error (Wei et al., 2020; Fan et al., 2024; Bai et al., 2024). Under these conditions, a refined cell can represent vegetation or terrain more accurately while still receiving forcing or hydrological process assumptions that are not equally refined. This explains why L-lai-landtypes improves the spatial pattern of runoff skill without producing uniform improvement everywhere.

These differences matter for how EarthMesh should be applied. Atmospheric refinement should prioritize smooth transition rows and dual-mesh quality. Ocean refinement should combine geometric constraints from coastlines with physical indicators such as eddy activity or bathymetric gradients. Land refinement should be tied to surface heterogeneity and to the scale of forcing data and hydrological process representation. A shared mesh-generation framework is useful because it provides users with a common construction logic, but the refinement criteria still need to align with the target model and process.

5.3 Advantages of an integrated meshing workflow

Compared with specialized unstructured mesh tools designed for single ESM components, EarthMesh's advantage lies in combining mesh generation, transition-zone construction, spring-based quality adjustment, and model-specific post-processing into a single workflow (**Table S5**). The framework generates multi-scale unstructured meshes for different ESM components (here MPAS-A, FVCOM, and CoLM2024) with a common construction logic, which provides a basis for cross-component coupling

https://doi.org/10.5194/egusphere-2026-6875
Preprint. Discussion started: 19 November 2026
© Author(s) 2026. CC BY 4.0 License.

studies (e.g., atmosphere–ocean, land–atmosphere, or ocean–land coupling), although coupled configurations are not tested in this study.

The post-processing step is another practical distinction. General-purpose mesh generators such as JIGSAW-GEO (Engwirda, 2017) mainly produce mesh geometry and connectivity, and model-oriented tools such as OceanMesh2D (Roberts et al., 2019) target a single model family. Users then need separate scripts to generate model-specific input files. This step is easy to underestimate. Atmospheric, oceanic, and land-surface models require different cell metadata, boundary information, and surface-property mappings. EarthMesh reduces this gap by generating input files for MPAS-A, FVCOM, and CoLM2024 using a common framework. This design improves reproducibility because the mesh construction and model initialization steps are recorded in a single workflow rather than being split across manual scripts.

5.4 Limitations and future work

The atmospheric and oceanic tests are idealized. They are useful because they isolate numerical behavior near resolution transitions, but real simulations introduce terrain, boundary conditions, physical parameterizations, and longer time scales. These factors can amplify errors that are not visible in a short, idealized integration. Future tests should evaluate EarthMesh under real-world regional climate simulations, coastal circulation experiments with realistic bathymetry, and coupled configurations in which feedback across components can stress the transition zones in different ways. Equally important, local refinement in atmospheric and oceanic variable-resolution experiments should shift from user-defined refinement to threshold-based refinement driven by bathymetric complexity, sea surface height variability, or other related metrics.

The land-surface experiment is also limited by the column-based structure of CoLM2024. As discussed in **Section 5.2**, the cells with reduced KGESS in L2 and L-lai-landtypes (**Figure 11**) likely reflect resolution-physics mismatch and missing lateral redistribution. Without lateral flow, refined land cells cannot represent the redistribution of water along hillslopes or river networks (Ji et al., 2017; Wei et al., 2020). With coarser atmospheric forcing, refined cells may also receive meteorological inputs that do not match their resolved surface features (Bai et al., 2024). Future EarthMesh

https://doi.org/10.5194/egusphere-2026-6875
Preprint. Discussion started: 19 November 2026
© Author(s) 2026. CC BY 4.0 License.

applications to land modeling should therefore be paired with higher-resolution forcing where available and with land models that include lateral hydrological processes.

The current spring-dynamics adjustment improves average mesh quality but does not guarantee that the worst cells improve monotonically. This limitation is pronounced in variable-resolution meshes with a single transition row, where the maximum angle of the atmospheric mesh (A-R2M1) decreases from 124.76° to 90.15° while that of the oceanic grid (O-R2M1) decreases from 127.28° to 90.43° , yet both remain above 90° (**Table S2 and S3**). For column-based land modeling, this is acceptable because the dual polygons can be constructed from centroids and do not require local orthogonality. For C-grid atmospheric modeling, the same geometry would be unsuitable. A worst-first optimization strategy could address this issue by targeting the lowest-quality elements before optimizing the full mesh (Engwirda, 2017; Logemann et al., 2021). Such a method would make the tool less dependent on the transition-row number when strict angle constraints are required.

A final direction is seamless land-river-ocean meshing. Current Earth system models often generate meshes separately for each component, which creates geometric and topological mismatches at component interfaces (Ward et al., 2020). Such mismatches are especially problematic for coastal compound flooding, where river discharge, storm surge, tides, and overland flow interact across the land-ocean boundary (Bao et al., 2022; Feng et al., 2024; Zhang and Yu, 2025). EarthMesh already provides a common construction framework for land and ocean meshes. Extending it to generate connected land-river-ocean grids would make the mesh itself part of the coupling strategy, rather than a set of separate component-specific inputs. This direction would move EarthMesh from a multi-component mesh generator toward a tool for interface-aware Earth system modeling.

6 Conclusions

EarthMesh provides a single workflow for generating variable-resolution unstructured meshes and model input files for multiple ESM components. In the three

https://doi.org/10.5194/egusphere-2026-6875
Preprint. Discussion started: 19 November 2026
© Author(s) 2026. CC BY 4.0 License.

tests, its VRMs reproduced baroclinic-wave structures, ocean eddy features, and runoff heterogeneity relative to fine uniform baselines. while using 8-47% of the cells. The land-surface experiment shows that physically adaptive refinement can approach the skill of uniform refinement with far fewer cells when the refinement criteria reflect the process being simulated. The results also point to the transition zone as the main geometric control on VRM behavior. EarthMesh combines a 5-7 vertex valence constraint with spring-dynamics optimization to smooth transitions in resolution. When only one transition row is used, however, obtuse triangles may remain, so C-grid applications should use multiple transition rows or a worst-first optimization option. EarthMesh offers solver-ready output for MPAS-A, FVCOM, and CoLM2024. Two development paths follow from the present results. One is to connect refined land meshes with forcing and physics that better represent lateral redistribution. The other is to extend EarthMesh toward seamless land-river-ocean meshes for coupled simulations at component interfaces.

Code and data availability

Drawing code, data, results, and models used can be found at https://doi.org/10.5281/zenodo.24009254 (Zhang, 2026a). The EarthMesh code is archived at https://doi.org/10.5281/zenodo.23827447 (Zhang, 2026b) and maintained at https://github.com/zhongwangwei/EarthMesh. The figures presented in this paper can be found in their original resolution at https://doi.org/10.5281/zenodo.23974439 (Zhang, 2026c). The soil and land-surface characteristic datasets are available at https://doi.org/10.1029/2019MS001784 (Dai et al., 2019), https://doi.org/10.3390/rs15071780 (Lin et al., 2023) and https://doi.org/10.1016/j.rse.2011.01.001 (Yuan et al., 2011), respectively. The IGBP land-cover dataset is available at https://doi.org/10.5067/MODIS/MCD12Q1.061 (Friedl and Sulla-Menashe, 2022). The canopy-height dataset is available at https://doi.org/10.3929/ETHZ-B-000609802 (Lang et al., 2022,2023), and the lake-coverage and lake-depth dataset is available at http://www.flake.igb-

https://doi.org/10.5194/egusphere-2026-6875
Preprint. Discussion started: 19 November 2026
© Author(s) 2026. CC BY 4.0 License.

673 berlin.de/data/gldbv2.tar.gz (Kourzeneva et al., 2012). ERA5-Land forcing is available
674 at https://doi.org/10.24381/CDS.E2161BAC (Copernicus Climate Change Service,
675 2019). GRFR discharge data are available at
676 https://doi.org/10.11888/Terre.tpdc.272901 (Yang et al., 2021).
677
678

679 **Financial support**

680 This work was supported by the Guangdong Major Project of Basic and Applied
681 Basic Research (grant 2021B0301030007), the Guangdong Basic and Applied Basic
682 Research Foundation (grants 2024A1515010283 and 2024A1515011760), the Southern
683 Marine Science and Engineering Guangdong Laboratory (Zhuhai) (SML2024SP008),
684 and the National Natural Science Foundation of China (grants 42475172, 42375166,
685 42375164, and 42575176). Additional support came from the National Key Scientific
686 and Technological Infrastructure project "Earth System Science Numerical Simulator
687 Facility" (EarthLab), the Innovation Platform for Academicians of Hainan Province
688 (YSPTZX202143), the Fundamental and Interdisciplinary Disciplines Breakthrough
689 Plan of the Ministry of Education of China (JYB2025XDXIM902), and the National
690 Key Research and Development Program of China (2024YFF0809000).
691
692

693 **Author contributions**

694 RZ and ZW conceived and designed the study, developed the model
695 implementation, performed the simulations, analysed the data, prepared the figures and
696 tables, and wrote the original manuscript. YL, HF and QX tested the model and edited
697 the paper. SZ, NW, XL, LL, HY, XL, SL and WS reviewed and revised the manuscript.
698 YD reviewed and revised the manuscript and provided project support and supervision.
699
700

701 **Competing interests**

702 The contact author has declared that none of the authors has any competing
703 interests.

https://doi.org/10.5194/egusphere-2026-6875
Preprint. Discussion started: 19 November 2026
© Author(s) 2026. CC BY 4.0 License.

Acknowledgments

We acknowledge high-performance computing support from the School of Atmospheric Sciences at Sun Yat-sen University. The authors used ChatGPT to improve language and readability, then reviewed and edited the manuscript and take responsibility for the final content. The authors are grateful to Darren Engwirda for his constructive comments, which significantly improved this work.

References

Bai, F., Wei, Z., Wei, N., Lu, X., Yuan, H., Zhang, S., Liu, S., Zhang, Y., Li, X., and Dai, Y.: Global Assessment of Atmospheric Forcing Uncertainties in The Common Land Model 2024 Simulations, J. Geophys. Res.-Atmos., 129, e2024JD041520, https://doi.org/10.1029/2024JD041520, 2024.

Bao, D., Xue, Z. G., Warner, J. C., Moulton, M., Yin, D., Hegermiller, C. A., Zambon, J.B. and He, R.: A numerical investigation of Hurricane Florence-induced compound flooding in the Cape Fear Estuary using a dynamically coupled hydrological-ocean model, J. Adv. Model. Earth Sy., 14, e2022MS003131, https://doi.org/10.1029/2022MS003131, 2022.

Barton, K. N., Pal, N., Brus, S. R., Petersen, M. R., Arbic, B. K., Engwirda, D., Roberts, A. F., Westerink, J. J., Wirasaet, D., and Schindelegger, M.: Global Barotropic Tide Modeling Using Inline Self-Attraction and Loading in MPAS-Ocean, J. Adv. Model. Earth Sy., 14, e2022MS003207, https://doi.org/10.1029/2022MS003207, 2022.

Chassignet, E. P., and Xu, X.: On the Importance of High-Resolution in Large-Scale Ocean Models, Adv. Atmos. Sci., 38, 1621–1634, https://doi.org/10.1007/s00376-021-0385-7, 2021.

Chen, C., Huang, H., Beardsley, R. C., Liu, H., Xu, Q., and Cowles, G.: A finite volume numerical approach for coastal ocean circulation studies: Comparisons with finite

https://doi.org/10.5194/egusphere-2026-6875
Preprint. Discussion started: 19 November 2026
© Author(s) 2026. CC BY 4.0 License.



difference models, J. Geophys. Res.-Oceans, 112, C03018, https://doi.org/10.1029/2006JC003485, 2007.

Chen, C., Liu, H., and Beardsley, R. C.: An Unstructured Grid, Finite-Volume, Three-Dimensional, Primitive Equations Ocean Model: Application to Coastal Ocean and Estuaries, J. Atmos. Ocean. Tech., 20, 159–186, https://doi.org/10.1175/1520-0426(2003)020<0159:AUGFVT>2.0.CO;2, 2003.

Conroy, C. J., Kubatko, E. J., and West, D. W.: ADMESH: An advanced, automatic unstructured mesh generator for shallow water models, Ocean Dyn., 62, 1503–1517, https://doi.org/10.1007/s10236-012-0574-0, 2012.

Copernicus Climate Change Service: ERA5-Land hourly data from 1950 to present [Dataset], Copernicus Climate Change Service (C3S) Climate Data Store (CDS), https://doi.org/10.24381/CDS.E2161BAC, 2019.

Dai, Y., Zeng, X., Dickinson, R. E., Baker, I., Bonan, G. B., Bosilovich, M. G., Denning, A. S., Dirmeyer, P. A., Houser, P. R., Niu, G., Oleson, K. W., Schlosser, C. A., and Yang, Z.-L.: The Common Land Model, B. Am. Meteorol. Soc., 84, 1013–1024, https://doi.org/10.1175/BAMS-84-8-1013, 2003.

Dai, Y., Xin, Q., Wei, N., Zhang, Y., Shangguan, W., Yuan, H., Zhang, S., Liu, S., and Lu, X.: A Global High-Resolution Data Set of Soil Hydraulic and Thermal Properties for Land Surface Modeling, J. Adv. Model. Earth Sy., 11, 2996–3023, https://doi.org/10.1029/2019MS001784, 2019.

Danilov, S. and Wang, Q.: Resolving eddies by local mesh refinement, Ocean Model., 93, 75–83, https://doi.org/10.1016/j.ocemod.2015.07.006, 2015.

Debreu, L., and Blayo, E.: Two-way embedding algorithms: a review, Ocean Dyn., 58, 415–428, https://doi.org/10.1007/s10236-008-0150-9, 2008.

Engwirda, D.: JIGSAW-GEO (1.0): locally orthogonal staggered unstructured grid generation for general circulation modelling on the sphere, Geosci. Model Dev., 10, 2117–2140, https://doi.org/10.5194/gmd-10-2117-2017, 2017.

Fan, H., Xu, Q., Bai, F., Wei, Z., Zhang, Y., Lu, X., Wei, N., Zhang, S., Yuan, H., Liu, S., Li, X., Li, X., and Dai, Y.: An Unstructured Mesh Generation Tool for Efficient High-Resolution Representation of Spatial Heterogeneity in Land Surface Models,

https://doi.org/10.5194/egusphere-2026-6875
Preprint. Discussion started: 19 November 2026
© Author(s) 2026. CC BY 4.0 License.

Geophys. Res. Lett., 51, e2023GL107059, https://doi.org/10.1029/2023GL107059, 2024.

Feng, D., Tan, Z., Engwirda, D., Wolfe, J. D., Xu, D., Liao, C., Bisht, G., Benedict, J. J., Zhou, T., and Li, H.-Y.: Simulation of compound flooding using river-ocean two-way coupled E3SM ensemble on variable-resolution meshes, J. Adv. Model. Earth Sy., 16, e2023MS004054, https://doi.org/10.1029/2023MS004054, 2024.

Friedl, M. and Sulla-Menashe, D.: MODIS/Terra+Aqua Land Cover Type Yearly L3 Global 500m SIN Grid V061 [Dataset], NASA Land Processes Distributed Active Archive Center, https://doi.org/10.5067/MODIS/MCD12Q1.061, 2022.

Hagos, S., Leung, R., Rauscher, S. A., and Ringler, T.: Error Characteristics of Two Grid Refinement Approaches in Aquaplanet Simulations: MPAS-A and WRF, Mon. Weather Rev., 141, 3022–3036, https://doi.org/10.1175/MWR-D-12-00338.1, 2013.

Hoch, K. E., Petersen, M. R., Brus, S. R., Engwirda, D., Roberts, A. F., Rosa, K. L., and Wolfram, P. J.: MPAS-Ocean Simulation Quality for Variable-Resolution North American Coastal Meshes, J. Adv. Model. Earth Sy., 12, e2019MS001848, https://doi.org/10.1029/2019MS001848, 2020.

Huang, L., Zhang, S., Niu, G., Wei, N., Yuan, H., Wei, Z., Lu, X., Peng, J., Li, W., and Dai, Y.: A Catchment-Based Hierarchical Spatial Tessellation Approach to a Better Representation of Land Heterogeneity for Hyper-Resolution Land Surface Modeling, Water Resour. Res., 58, e2021WR031589, https://doi.org/10.1029/2021WR031589, 2022.

Jablonowski, C., and Williamson, D. L.: A baroclinic instability test case for atmospheric model dynamical cores, Q. J. Roy. Meteor. Soc., 132, 2943–2975, https://doi.org/10.1256/qj.06.12, 2006.

Jacobsen, D. W., Gunzburger, M., Ringler, T., Burkardt, J., and Peterson, J.: Parallel algorithms for planar and spherical Delaunay construction with an application to centroidal Voronoi tessellations, Geosci. Model Dev., 6, 1353–1365, https://doi.org/10.5194/gmd-6-1353-2013, 2013.

Ji, P., Yuan, X., and Liang, X.-Z.: Do Lateral Flows Matter for the Hyperresolution

https://doi.org/10.5194/egusphere-2026-6875
Preprint. Discussion started: 19 November 2026
© Author(s) 2026. CC BY 4.0 License.

Land Surface Modeling? J. Geophys. Res.-Atmos., 122, 12077–12092, https://doi.org/10.1002/2017JD027366, 2017.

Klemp, J. B.: A Terrain-Following Coordinate with Smoothed Coordinate Surfaces, Mon. Weather Rev., 139, 2163–2169, https://doi.org/10.1175/MWR-D-10-05046.1, 2011.

Knoben, W. J. M., Freer, J. E., and Woods, R. A.: Technical note: Inherent benchmark or not? Comparing Nash–Sutcliffe and Kling–Gupta efficiency scores, Hydrol. Earth Syst. Sci., 23, 4323–4331, https://doi.org/10.5194/hess-23-4323-2019, 2019.

Kourzeneva, E., Asensio, H., Martin, E., and Faroux, S.: Global gridded dataset of lake coverage and lake depth for use in numerical weather prediction and climate modelling, Tellus A, 64, 15640, https://doi.org/10.3402/tellusa.v64i0.15640, 2012.

Lambrechts, J., Comblen, R., Legat, V., Geuzaine, C., and Remacle, J.-F.: Multiscale mesh generation on the sphere, Ocean Dyn., 58, 461-473, https://doi.org/10.1007/s10236-008-0148-3, 2008.

Lang, N., Schindler, K., and Wegner, J. D.: ETH_GlobalCanopyHeight_10m_2020_version1: Global canopy height map for the year 2020 derived from Sentinel-2 and GEDI [Dataset], ETH Zurich, https://doi.org/10.3929/ETHZ-B-000609802, 2022.

Lang, N., Jetz, W., Schindler, K., and Wegner, J. D.: A high-resolution canopy height model of the Earth, Nat. Ecol. Evol., 7, 1778–1789, https://doi.org/10.1038/s41559-023-02206-6, 2023.

Lin, W., Yuan, H., Dong, W., Zhang, S., Liu, S., Wei, N., Lu, X., Wei, Z., Hu, Y., and Dai, Y.: Reprocessed MODIS Version 6.1 Leaf Area Index Dataset and Its Evaluation for Land Surface and Climate Modeling, Remote Sens., 15, 1780, https://doi.org/10.3390/rs15071780, 2023.

Logemann, K., Linardakis, L., Korn, P., and Schrum, C.: Global tide simulations with ICON-O: testing the model performance on highly irregular meshes, Ocean Dyn., 71, 43–57, https://doi.org/10.1007/s10236-020-01428-7, 2021.

Loveland, T. R., Reed, B. C., Brown, J. F., Ohlen, D. O., Zhu, Z., Yang, L., and Merchant, J. W.: Development of a global land cover characteristics database and

https://doi.org/10.5194/egusphere-2026-6875
Preprint. Discussion started: 19 November 2026
© Author(s) 2026. CC BY 4.0 License.

IGBP DISCover from 1 km AVHRR data, Int. J. Remote Sens., 21, 1303–1330. https://doi.org/10.1080/014311600210191, 2000.

Marsh, C. B., Pomeroy, J. W., Spiteri, R. J., and Wheater, H. S.: A finite volume blowing snow model for use with variable resolution meshes, Water Resour. Res., 56, e2019WR025307, https://doi.org/10.1029/2019WR025307, 2020.

Marsh, C. B., Spiteri, R. J., Pomeroy, J. W., and Wheater, H. S.: Multi-objective unstructured triangular mesh generation for use in hydrological and land surface models, Comput. Geosci., 119, 49–67, https://doi.org/10.1016/j.cageo.2018.06.009, 2018.

Iga, S.-I., and Tomita, H.: Improved smoothness and homogeneity of icosahedral grids using the spring dynamics method, J. Comput. Phys., 258, 208-226, https://doi.org/10.1016/j.jcp.2013.10.013, 2014.

Park, S.-H., Skamarock, W. C., Klemp, J. B., Fowler, L. D., and Duda, M. G.: Evaluation of global atmospheric solvers using extensions of the Jablonowski and Williamson baroclinic wave test case, Mon. Weather Rev., 141, 3116–3129, https://doi.org/10.1175/MWR-D-12-00096.1, 2013.

Ringler, T. D., Jacobsen, D., Gunzburger, M., Ju, L., Duda, M., and Skamarock, W.: Exploring a multiresolution modeling approach within the shallow-water equations, Mon. Weather Rev., 139, 3348–3368, https://doi.org/10.1175/MWR-D-10-05049.1, 2011.

Ringler, T., Petersen, M., Higdon, R. L., Jacobsen, D., Jones, P. W., and Maltrud, M.: A multi-resolution approach to global ocean modeling, Ocean Model., 69, 211–232, https://doi.org/10.1016/j.ocemod.2013.04.010, 2013.

Roberts, K. J., Pringle, W. J., and Westerink, J. J.: OceanMesh2D 1.0: MATLAB-based software for two-dimensional unstructured mesh generation in coastal ocean modeling, Geosci. Model Dev., 12, 1847–1868, https://doi.org/10.5194/gmd-12-1847-2019, 2019.

Sein, D. V., Danilov, S., Biastoch, A., Durgadoo, J. V., Sidorenko, D., Harig, S., and Wang, Q.: Designing variable ocean model resolution based on the observed ocean variability, J. Adv. Model. Earth Sy., 8, 904–

https://doi.org/10.5194/egusphere-2026-6875
Preprint. Discussion started: 19 November 2026
© Author(s) 2026. CC BY 4.0 License.

916, https://doi.org/10.1002/2016MS000650, 2016.

Sein, D. V., Koldunov, N. V., Danilov, S., Wang, Q., Sidorenko, D., Fast, I., Rackow, T., Cabos, W., and Jung, T.: Ocean modeling on a mesh with resolution following the local Rossby radius, J. Adv. Model. Earth Sy., 9, 2601–2614, https://doi.org/10.1002/2017MS001099, 2017.

Skamarock, W. C., Klemp, J. B., Duda, M. G., Fowler, L. D., Park, S.-H., and Ringler, T. D.: A Multiscale Nonhydrostatic Atmospheric Model Using Centroidal Voronoi Tesselations and C-Grid Staggering, Mon. Weather Rev., 140, 3090–3105, https://doi.org/10.1175/MWR-D-11-00215.1, 2012.

Song, P., Sidorenko, D., Scholz, P., Thomas, M., and Lohmann, G.: The tidal effects in the Finite-volumE Sea ice–Ocean Model (FESOM2.1): A comparison between parameterised tidal mixing and explicit tidal forcing, Geosci. Model Dev., 16, 383–405, https://doi.org/10.5194/gmd-16-383-2023, 2023.

Tesfa, T. K., Leung, L. R., and Ghan, S. J.: Exploring topography-based methods for downscaling subgrid precipitation for use in Earth System models, J. Geophys. Res.-Atmos, 125, e2019JD031456, https://doi.org/10.1029/2019jd031456, 2020.

Tomita, H., Satoh, M., and Goto, K.: An Optimization of the Icosahedral Grid Modified by Spring Dynamics, J. Comput. Phys., 183, 307–331, https://doi.org/10.1006/jcph.2002.7193, 2002.

Walko, R. L., and Avissar, R.: The Ocean–Land–Atmosphere Model (OLAM). Part I: Shallow-water tests, Mon. Weather Rev., 136, 4033–4044, https://doi.org/10.1175/2008MWR2522.1, 2008.

Walko, R. L., and Avissar, R.: A Direct Method for Constructing Refined Regions in Unstructured Conforming Triangular–Hexagonal Computational Grids: Application to OLAM, Mon. Weather Rev., 139, 3923–3937, https://doi.org/10.1175/MWR-D-11-00021.1, 2011.

Wang, N., and Lee, J.-L.: Geometric properties of the icosahedral-hexagonal grid on the two-sphere, SIAM J. Sci. Comput., 33, 2536-2559, https://doi.org/10.1137/090761355, 2011.

Wang, Q., Danilov, S., Sidorenko, D., Timmermann, R., Wekerle, C., Wang, X., Jung,

https://doi.org/10.5194/egusphere-2026-6875
Preprint. Discussion started: 19 November 2026
© Author(s) 2026. CC BY 4.0 License.

T., and Schröter, J.: The Finite Element Sea Ice-Ocean Model (FESOM) v.1.4: formulation of an ocean general circulation model, Geosci. Model Dev., 7, 663-693, https://doi.org/10.5194/gmd-7-663-2014, 2014.

Ward, N. D., Megonigal, J. P., Bond-Lamberty, B., Bailey, V. L., Butman, D., Canuel, E. A., Diefenderfer, H., Ganju, N. K., Goñi, M. A., Graham E. B., Hopkinson, C. S., Khangaonkar, T., Langley, J. A., McDowell, N. G., Myers-Pigg, A. N., Neumann, R. B., Osburn, C. L., Price, R. M., Rowland, J., Sengupta, A., Simard, M., Thornton, P. E., Tzortziou, M., Vargas, R., Weisenhorn, P. B., and Windham-Myers, L.: Representing the function and sensitivity of coastal interfaces in Earth system models, Nat. Commun., 11, 2458, https://doi.org/10.1038/s41467-020-16236-2, 2020.

Wei, Z., He, X., Zhang, Y., Pan, M., Sheffield, J., Peng, L., Yamazaki, D., Moiz, A., Liu, Y., and Ikeuchi, K.: Identification of uncertainty sources in quasi-global discharge and inundation simulations using satellite-based precipitation products, J. Hydrol., 589, 125180, https://doi.org/10.1016/j.jhydrol.2020.125180, 2020.

Wei, Z., Fang, G., Xu, T., Wang, Y., and Lian, Z.: Seasonal variability of the isopycnal surface circulation in the South China Sea derived from a variable-grid global ocean circulation model, Acta Oceanol. Sin., 35, 11-20, https://doi.org/10.1007/s13131-016-0791-3, 2016.

Wicker, L. J., and Skamarock, W. C.: Time-Splitting Methods for Elastic Models Using Forward Time Schemes, Mon. Weather Rev., 130, 2088–2097, https://doi.org/10.1175/1520-0493(2002)130<2088:TSMFEM>2.0.CO;2, 2002.

Xu, M., Zhao, C., Gu, J., Feng, J., Hagos, S., Leung, L. R., Luo, Y., Guo, J., Li, R., and Fu, Y.: Convection-permitting hindcasting of diurnal variation of Mei-yu rainfall over East China with a global variable-resolution model, J. Geophys. Res.-Atmos., 126, e2021JD034823, https://doi.org/10.1029/2021JD034823, 2021.

Yang, Y., Pan, M., Lin, P., Beck, H. E., Zeng, Z., Yamazaki, D., David, C. H., Lu, H., Yang, K., Hong, Y., and Wood, E. F.: Global Reach-Level 3-Hourly River Flood Reanalysis (1980–2019), B. Am. Meteorol. Soc., 102, E2086–E2105, https://doi.org/10.1175/BAMS-D-20-0057.1, 2021.

https://doi.org/10.5194/egusphere-2026-6875
Preprint. Discussion started: 19 November 2026
© Author(s) 2026. CC BY 4.0 License.



914 Yuan, H., Dai, Y., Xiao, Z., Ji, D., and Shangguan, W.: Reprocessing the MODIS Leaf
915 Area Index products for land surface and climate modelling, Remote Sens.
916 Environ., 115, 1171–1187, https://doi.org/10.1016/j.rse.2011.01.001, 2011.
917 Zängl, G., Reinert, D., and Prill, F.: Grid refinement in ICON v2.6.4, Geosci. Model
918 Dev., 15, 7153–7176, https://doi.org/10.5194/gmd-15-7153-2022, 2022.
919 Zängl, G., Reinert, D., Rípodas, P., and Baldauf, M.: The ICON (ICOsahedral
920 Nonhydrostatic) modelling framework of DWD and MPI-M: Description of the
921 nonhydrostatic dynamical core, Q. J. Roy. Meteor. Soc., 141, 563–579,
922 https://doi.org/10.1002/qj.2378, 2015.
923 Zhang, A. and Yu, X.: Development of a land–river–ocean coupled model for
924 compound floods jointly caused by heavy rainfall and storm surges in large river
925 delta regions, Hydrol. Earth. Syst Sci., 29, 2505–2520,
926 https://doi.org/10.5194/hess-29-2505-2025, 2025.
927 Zhou, Y., Zhang, Y., Li, J., Yu, R., and Liu, Z.: Configuration and evaluation of a global
928 unstructured mesh atmospheric model (GRIST-A20.9) based on the variable-
929 resolution approach, Geosci. Model Dev., 13, 6325-
930 6348, https://doi.org/10.5194/gmd-13-6325-2020, 2020.
931 Zhang, R.: Drawing code, data, results, and models used in “EarthMesh: A Multi-scale
932 Unstructured Mesh Generation Tool for Earth System Models” (version 4)
933 [Dataset], Zenodo, https://doi.org/10.5281/zenodo.24009254, 2026a.
934 Zhang, R.: Code of EarthMesh, an unstructured mesh generation tool for Earth System
935 Models (Version 1) [Software],
936 Zenodo, https://doi.org/10.5281/zenodo.23827447, 2026b.
937 Zhang, R.: High quality figures of “EarthMesh: A Multi-scale Unstructured Mesh
938 Generation Tool for Earth System Models” (version 1) [Figure], Zenodo,
939 https://doi.org/10.5281/zenodo.23974439, 2026c.